J. Fluid Mech. (2006), *vol.* 558, *pp.* 451–475.
doi:10.1017/S002211200600022X Printed in the United Kingdom

The viscous drag of spheres and filaments moving in membranes or monolayers

By TH. M. FISCHER[1], P. DHAR[1] AND P. HEINIG[2]

[1]Department of Chemistry and Biochemistry, The Florida State University, Tallahassee, FL 32306-4390, USA
tfischer@chem.fsu.edu

[2]Laboratoire de Physique des Solides, UMR 8502-Université Paris-Sud, Bat. 510, 91405 Orsay, France

(Received 2 August 2004 and in revised form 9 November 2005)

We numerically calculate the drag on a sphere or a filament immersed in an incompressible viscous monolayer or membrane on one, or between two, viscous infinitely deep bulk phases. We show that contributions due to the Marangoni effect of the monolayer or membrane account for a significant part of the total drag. Effects of protrusion of objects into the three-dimensional fluids adjacent to the monolayer and membrane are investigated. Known analytical expressions in the limit of a very viscous membrane or monolayer are recovered by our numerics. A sphere in a membrane exhibits maximal drag when symmetrically immersed with the equator coinciding with the membrane plane. No discontinuity of the drag arises when the sphere is totally immersed into the subphase and detaches from the monolayer. Effects of protrusion are more important for objects moving in a membrane or monolayer of low surface viscosity. At large surface shear viscosity protrusions must be larger than the length defined by the ratio of surface to bulk viscosities to alter the drag on the object. Our calculations may be useful for the measurement of hydrodynamic radii of lipid rafts in membranes and for electrocapillary effects of spheres immersed in a surface.

1. Introduction

The use of colloidal particles as tracer particles for the investigation of the rheological properties of interfaces has received considerable attention over the past decade. Spherical particles have been immersed in Langmuir monolayers at the air/water interface (Petkov *et al.* 1995; Forstner, Käs & Martin 2001; Forstner *et al.* 2003; Sickert & Rondelez 2003, 2004; Fischer 2004), in lipid bilayers in the form of giant vesicles (Dimova *et al.* 1999*a*; Dimova, Dietrich & Pouligny 1999*b*; Dimova *et al.* 2000), and in polarized biological cells where they were coupled to the plasma membrane (Pralle *et al.* 2000). The colloidal particles exert forces on the three-dimensional fluids and the interface that separates them. These forces lead to mechanical responses of both the fluids and the interface in the form of three- and two-dimensional flow and pressure fields acting back onto the particle. Analytical and numerical calculations on the problem of a sphere moving in an interface have been pioneered by Danov *et al.* (1995), who refined the work (Danov, Dimova & Pouligny 2000). However, in their analysis Danov *et al.* (1995, 2000) consider only viscous responses of the interface and neglect Marangoni effects. Marangoni stress is a tangential surface stress generated by gradients in surface density of surfactants. This stress becomes most pronounced in the limit of vanishing surface compressibility

$\kappa_s \eta a \dot{\gamma} \ll 1$ (κ_s being the surface compressibility, η the three-dimensional viscosity, a the radius of the object moving in the interface and $\dot{\gamma}$ the shear rate). In this limit the Marangoni effects are simply incorporated into the theoretical description by approximating the surface or interface as incompressible.

Marangoni effects often dominate over viscous effects as has been theoretically predicted by Saffman & Delbrück (1975), Hughes, Pailthorpe & White (1981) and Stone & Ajdari (1998) and experimentally confirmed by Peters & Cherry (1982) for proteins undergoing Brownian motion in membranes and by Klingler & McConnell (1993), Schwartz, Knobler & Bruinsma (1994), Steffen *et al.* (2001), and Wurlitzer, Schmiedel & Fischer (2002) for the motion of flat, circular objects embedded in a monolayer. Indeed, for particles in the micron range and below, the approximation of the monolayer (membrane) interface as an incompressible two-dimensional viscous liquid is a good description of the behaviour of such monolayers (membranes), even if the surfactant concentration in the interface is so low that the amphiphiles are in a two-dimensional ideal gaseous phase.

Characteristic features of the incompressibility of the interface are logarithmic correction terms in the translational drag coefficients both in the high and low viscosity limits. Experiments evaluated with the formulae given by Danov *et al.* (1995, 2000) that lack these characteristics therefore lead to overestimation by an order of magnitude of the surface viscosity (Petkov *et al.* 1995; Dimova *et al.* 1999*a*, *b*, 2000; Sickert & Rondelez 2003, 2004) or an underestimation of the hydrodynamic radius of rafts (Pralle *et al.* 2000) to which the colloidal beads are coupled. Sickert & Rondelez (2003, 2004) attempted to overcome the deficiencies by evaluating the Brownian motion of colloidal beads in a monolayer using Danov *et al.*'s theory with a renormalized bulk viscosity. However, there is no physical justification for such a renormalization. To enable proper data evaluation of particle tracking experiments correct formulae without the deficiencies mentioned above are needed. The present work incorporates Marangoni forces into the treatment of a sphere immersed in a monolayer or a membrane by solving the equations for an incompressible interface. The work is a logical extension of the description of two-dimensional objects immersed in a membrane given by Saffmann & Delbrück (1975), Hughes *et al.* (1981) and Stone & Ajdari (1998) to three-dimensional objects that protrude into the three-dimensional fluid and complementary to work of Stone (2005, personal communication) that solves the problem as a perturbation series in the protrusion. The spheres in a creeping flow can both translate and rotate. Both translation and rotation require a torque and force that are proportional to a linear combination of the translational and angular velocity of the sphere. It is the task of the current work to compute the constants of proportionality, i.e. the translational, rotational and coupling drag coefficients, defined in § 3 for objects incorporated in or near a two-dimensional interface of surface shear viscosity η_s that is bounded by liquids of different or similar bulk viscosities η_1 and η_2.

2. Hydrodynamic drag on objects of arbitrary shape

Consider a solid three-dimensional object moving in a monolayer (membrane) of surface shear viscosity η_s between two laterally infinitely extended viscous phases (figure 1). The flow of the subphase is described by Stokes' equation and the continuity equation:

$$\left.\begin{aligned} \boldsymbol{f} - \nabla p + \eta \Delta \boldsymbol{u} = 0, \\ \nabla \cdot \boldsymbol{u} = 0, \end{aligned}\right\} \tag{2.1}$$

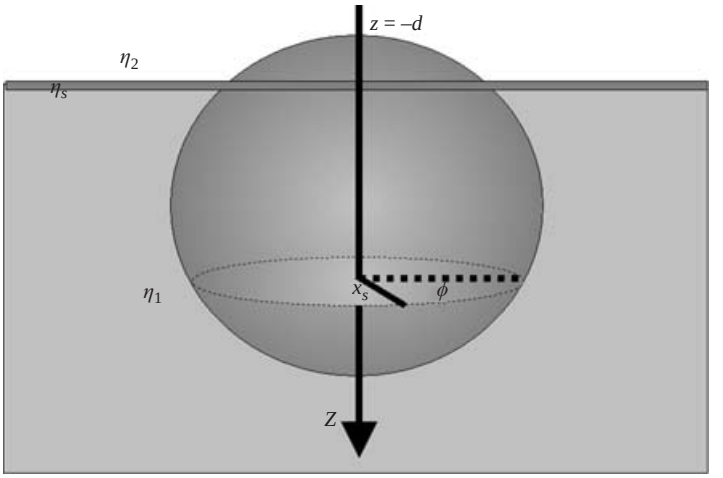

FIGURE 1. Sketch of a sphere immersed in a surface of viscosity η_s between two liquids of infinite depth and viscosity η_1 and η_2.

where $\boldsymbol{f}$ is an external force, p is the lower-phase pressure, $\boldsymbol{u}$ denotes the subphase velocity and

$$\eta(z) = \eta_1 \Theta(-z) + \eta_2 \Theta(z) \tag{2.2}$$

is the viscosity that is η_1 for $z < 0$ in the subphase and η_2 for $z > 0$ in the upper phase. $\Theta(z)$ is the Heaviside function. The dynamic stress tensor is given by

$$\boldsymbol{\sigma} = -p\mathbf{1} + \eta(\nabla \boldsymbol{u} + [\nabla \boldsymbol{u}]^t), \tag{2.3}$$

where $\mathbf{1}$ denotes the unit tensor in three-dimensional space. The monolayer (membrane) surface A is assumed to be flat and located at the position $z = 0$ and no deformation of the surface by e.g. electrocapillary effects (Nikolaides *et al.* 2002; Danov, Kralchevsky & Boneva 2004) is assumed. Such an approximation is reasonable if the viscous drag is small compared to capillary stresses ($\eta U/\sigma_s \ll 1$, U being the speed of the object, σ_s the tension of the monolayer/membrane). For optical tweezer experiments in Langmuir monolayers typical values of this ratio are of the order of $\eta U/\sigma_s \approx 10^{-6}$. The tension of membranes is much lower than the air/water tension; however, for membranes the liquid is usually the same on both sides leading to a symmetric immersion in the membrane and deformations play no role for symmetry reasons. The assumption of a flat interface is therefore reasonable for the case of colloidal particles in Langmuir monolayers as well as for biological membranes. The flatness of the interface under such conditions also leads to the effect that the rotation of a sphere is strongly suppressed when it is immersed in it since rotation of a sphere in a flat interface leads to a divergent stress near the contact line that forbids its rotation (O'Neill, Ranger & Brenner 1986; Huh & Scriven 1971; Dussan V. & Davis 1974). Hence no rotation of the sphere occurs at the level of this approximation once it touches the interface. The area of the surface of the three-dimensional object touching the liquid or the monolayer is denoted by ∂O. At both surfaces, boundary conditions have to be fulfilled. At the surface ∂O of the three-dimensional object, the velocity of the liquid must coincide with the velocity $U\boldsymbol{e}_x$ of the object (non-slip

boundary condition):

$$\boldsymbol{u} = U\boldsymbol{e}_x \qquad \text{for} \quad \boldsymbol{x} \in \partial\boldsymbol{O}, \tag{2.4}$$

while at the monolayer covered surface A, the flow can be approximated by an incompressible two-dimensional Stokes flow:

$$\nabla_s \cdot \boldsymbol{u}_s = 0 \qquad \text{for} \quad \boldsymbol{x}_s \in A, \tag{2.5}$$

$$\boldsymbol{u}_z(z=0) = 0 \qquad \text{for} \quad \boldsymbol{x}_s \in A, \tag{2.6}$$

$$\boldsymbol{f}_s - \nabla_s \pi_s + \eta_s \Delta_s \boldsymbol{u}_s + \left\| \eta \frac{\partial \boldsymbol{u}}{\partial z} \right\|_s = 0 \qquad \text{for} \quad \boldsymbol{x}_s \in A, \tag{2.7}$$

where $\boldsymbol{f}_s$ is an external surface force parallel to the monolayer (membrane) surface, π_s is the surface pressure, $\boldsymbol{u}_s$ is the surface velocity, and ∇_s denotes the surface gradient. The symbol $\|C\|_s = C(z=+0) - C(z=-0)$ denotes the jump in C across the interface.

The approximation of the interface as incompressible is justified since surface compression waves travel with the speed of surface phonons, which is much larger than the speed of the object. Hence Marangoni forces are transmitted instantaneously in this approximation. The cause of these Marangoni forces are small surfactant density gradients that drop out of the equations in the limit of vanishing compressibility. The incompressibility of the surface is a widely accepted approximation that has been introduced in the work of Saffmann & Delbrück (1975), Hughes *et al.* (1981) and Stone & Ajdari (1998). In the work of Danov *et al.* (1995, 2000) this approximation has been replaced by the condition of a constant surface pressure that neglects the Marangoni forces. The difference of the theory presented here to the work of Danov *et al.* (1995, 2000) therefore is to put the theory of protruding objects into the same framework as Saffmann & Delbrück (1975), Hughes *et al.* (1981) and Stone & Ajdari (1998) who treat non-protruding objects at an interface.

The surface dynamic stress tensor is given by

$$\boldsymbol{\sigma}_s = -\pi_s \boldsymbol{I}_s + \eta_s(\nabla_s \boldsymbol{u}_s + [\nabla_s \boldsymbol{u}_s]^t). \tag{2.8}$$

Here, $\boldsymbol{I}_s = \mathbf{1} - \boldsymbol{e}_z\boldsymbol{e}_z$ denotes the projector onto the monolayer (membrane) surface. We may construct a solution for an arbitrary object immersed in the bulk phases and the interface from the solution for a point force source

$$\boldsymbol{f} = \boldsymbol{F}\,\delta^3(\boldsymbol{x} - h\boldsymbol{e}_z), \quad \boldsymbol{f}_s = 0, \tag{2.9}$$

located at a distance h from the monolayer (membrane) surface. The bulk solution to (2.1) can be written as (Russel, Saville & Schowalter 1989)

$$\left.\begin{aligned} \boldsymbol{u}(x) &= \int_{|R^3/V} \mathrm{d}^3\boldsymbol{x}'\, \boldsymbol{O}_0(\boldsymbol{x} - \boldsymbol{x}') \cdot \boldsymbol{f}_0(\boldsymbol{x}') \\ \boldsymbol{O}_0(\boldsymbol{r}) &= \frac{1}{8\pi\eta}\left(\frac{\mathbf{1}}{r} + \frac{\boldsymbol{r}\boldsymbol{r}}{r^3}\right) \\ p(\boldsymbol{x}) &= \int_{|R^3/V} \mathrm{d}^3\boldsymbol{x}' \frac{\boldsymbol{x} - \boldsymbol{x}'}{4\pi|\boldsymbol{x} - \boldsymbol{x}'|^3} \cdot \boldsymbol{f}_0(\boldsymbol{x}') \end{aligned}\right\} \tag{2.10}$$

where $\boldsymbol{O}_0$ is the bulk Oseen tensor, $\boldsymbol{r} = \boldsymbol{x} - \boldsymbol{x}'$ is the vector pointing from $\boldsymbol{x}'$ toward $\boldsymbol{x}$, $\boldsymbol{f}_0(\boldsymbol{x}')$ is a force density, which is non-zero on the complement of the volume where the Stokes equation holds. Similarly, for a surface force $\boldsymbol{f}_s$ in the monolayer

(membrane) we find (Levine & MacKintosh 2002; Fischer 2003):

$$\boldsymbol{u}(x) = \int_{|R^2/A} \mathrm{d}^2\boldsymbol{x}'_s \boldsymbol{O}_s(\boldsymbol{x} - \boldsymbol{x}'_s) \cdot \boldsymbol{f}_s(\boldsymbol{x}'_s), \tag{2.11a}$$

$$\boldsymbol{O}_s(\boldsymbol{r}) = \frac{4}{8\pi(\eta_1+\eta_2)} \sum_{n=0}^{\infty} \left(\mathscr{B}a \frac{\partial}{\partial|z|}\right)^n \left[\left(\frac{|z|}{r_s^2} - \frac{z^2}{r_s^2\left(r_s^2+z^2\right)^{1/2}}\right) \times \left[\boldsymbol{I}_s - \frac{\boldsymbol{r}_s\boldsymbol{r}_s}{r_s^2}\right] + \frac{\left(r_s^2+z^2\right)^{1/2} - |z|}{r_s^2} \frac{\boldsymbol{r}_s\boldsymbol{r}_s}{r_s^2}\right] \quad \text{for} \quad z \neq 0, \tag{2.11b}$$

$$\boldsymbol{O}_s(\boldsymbol{r}_s) = \frac{2\boldsymbol{r}_s\boldsymbol{r}_s - \boldsymbol{I}_s r_s^2}{r_s^2} \frac{1}{4(\eta_1+\eta_2)r_s} \left\{ \boldsymbol{H}_1\left(\frac{r_s}{\mathscr{B}a}\right) - N_1\left(\frac{r_s}{\mathscr{B}a}\right) - \frac{2\mathscr{B}a}{\pi r_s} \right\} + \frac{r_s^2\boldsymbol{I}_s - \boldsymbol{r}_s\,\boldsymbol{r}_s}{r_s^2} \frac{1}{4(\eta_1+\eta_2)\mathscr{B}a} \left\{ \boldsymbol{H}_0\left(\frac{r_s}{\mathscr{B}a}\right) - N_0\left(\frac{r_s}{\mathscr{B}a}\right) \right\}, \tag{2.11c}$$

$$\pi_s(\boldsymbol{x}_s) = \int \mathrm{d}^2\boldsymbol{x}'_s \frac{\boldsymbol{x}_s - \boldsymbol{x}'_s}{2\pi|\boldsymbol{x}_s - \boldsymbol{x}'_s|^2} \cdot \boldsymbol{f}_s(\boldsymbol{x}'_s), \tag{2.11d}$$

$$p(\boldsymbol{x}) = 0, \tag{2.11e}$$

where $\boldsymbol{H}_n$, N_n are Struve functions, and Bessel functions of the second kind of the order n (Gradshteyn & Ryshik 1981, § 8.550, 8.403),

$$\mathscr{B} = \frac{\eta_s}{(\eta_1+\eta_2)a} \tag{2.12}$$

is Boussinesq's number, a is a typical length scale of the 3D object, and $\boldsymbol{x}_s = \boldsymbol{I}_s \cdot \boldsymbol{x}$. We would like to solve Stokes equation for a point force placed at a distance h from the surface and subject to the boundary conditions (2.5)–(2.7) and (2.9). In order to do so, we start with the ansatz

$$\boldsymbol{u}(x) = \Theta(z \cdot z') \int \mathrm{d}^3\boldsymbol{x}' \boldsymbol{O}_0(\boldsymbol{x} - \boldsymbol{x}') \cdot \tilde{\boldsymbol{f}}(x') + \int \mathrm{d}^2\boldsymbol{x}'_s \boldsymbol{O}_s(\boldsymbol{x} - \boldsymbol{x}'_s) \cdot \tilde{\boldsymbol{f}}_s(\boldsymbol{x}'_s) \tag{2.13}$$

with a bulk force of the form

$$\tilde{\boldsymbol{f}}(x) = \boldsymbol{F}\delta^3(\boldsymbol{x} - h\boldsymbol{e}_z) - [\boldsymbol{I}_s - \boldsymbol{e}_z\boldsymbol{e}_z] \cdot \boldsymbol{F}\delta^3(\boldsymbol{x} + h\boldsymbol{e}_z) + G_z(\boldsymbol{x}_s)\boldsymbol{e}_z\delta(z). \tag{2.14}$$

The Heaviside function $\Theta(z \cdot z')$ ensures that bulk forces only cause flow in the liquid on the same side of the membrane as the force. The flow on the other side is caused purely by surface forces in the membrane. The first term in (2.14) is the solution of the inhomogeneous Stokes equation in the phase where the point force is located. The second term is a virtual image force source chosen in such a way as to ensure that the force and image force generate an incompressible flow (equation (2.5)) at the surface $z = 0$. The third term, which satisfies equation (2.5), must be chosen such that the normal component of the velocity (2.13) vanishes at the surface (equation (2.6)). The second term in (2.13), which satisfies both equations (2.5) and (2.6), must then be chosen to counterbalance the lateral surface forces generated by the first term. For the determination of the force densities G_z and $\tilde{\boldsymbol{f}}_s$, it is useful to change to Fourier space,

$$\hat{a}(q) = \int a(\boldsymbol{x}) \mathrm{e}^{\mathrm{i}q\cdot x} \mathrm{d}^3\boldsymbol{x} \tag{2.15}$$

where we split the wave vector

$$\boldsymbol{q} = \boldsymbol{q}_s + q_z\boldsymbol{e}_z \tag{2.16}$$

into components tangential and normal to the surface. It is also useful to note that the surface Fourier transformation of any interfacial function can be written as

$$\check{a}(\boldsymbol{q}_s) := \frac{1}{2\pi}\int \hat{a}(\boldsymbol{q})\,\mathrm{d}q_z = \int a(\boldsymbol{x}_s, z=0)\mathrm{e}^{\mathrm{i}\boldsymbol{q}_s\cdot\boldsymbol{x}_s}\mathrm{d}^2\boldsymbol{x}_s. \tag{2.17}$$

Using these definitions we find

$$\hat{\check{\boldsymbol{f}}}(\boldsymbol{q}) = (2\cos(q_z h)F_z + \check{G}_z(\boldsymbol{q}_s))\boldsymbol{e}_z + 2\mathrm{i}\sin(q_z h)\boldsymbol{F}_s \tag{2.18}$$

where $\boldsymbol{F}_s = \boldsymbol{I}_s\cdot\boldsymbol{F}$ and $F_z = \boldsymbol{e}_z\cdot\boldsymbol{F}$. The velocity and pressure are found as

$$\hat{\boldsymbol{u}}(\boldsymbol{q}) = \frac{1}{\eta q^4}(q^2\mathbf{1}-\boldsymbol{q}\boldsymbol{q})\cdot\hat{\check{\boldsymbol{f}}}(\boldsymbol{q}) + 2\frac{q_s^2\boldsymbol{I}_s - \boldsymbol{q}_s\,\boldsymbol{q}_s}{(\eta_1+\eta_2)q^2q_s^2(1+\mathscr{B}q_s a)}\mathrm{e}^{-\mathrm{i}q_z\epsilon+q_s\epsilon}\cdot\check{\check{\boldsymbol{f}}}_s(\boldsymbol{q}_s), \tag{2.19a}$$

$$\hat{p}(\boldsymbol{q}) = \mathrm{i}\frac{\boldsymbol{q}}{q^2}\cdot\hat{\check{\boldsymbol{f}}}(\boldsymbol{q}), \tag{2.19b}$$

$$\check{\pi}_s(\boldsymbol{q}_s) = \mathrm{i}\frac{\boldsymbol{q}_s}{q_s^2}\cdot\check{\check{\boldsymbol{f}}}_s(\boldsymbol{q}_s), \tag{2.19c}$$

Here ϵ is a small but positive length that ensures that the velocity is differentiable at $z=0$. The normal component of the velocity at $z=0$ is found with the use of equation (2.17):

$$\check{u}_z(\boldsymbol{q}_s) = \frac{1}{4\eta q_s}(2(1+q_s h)\mathrm{e}^{-q_s h}F_z + \check{G}_z(\boldsymbol{q}_s)) - \mathrm{i}\frac{1}{4\eta q_s}2\mathrm{e}^{-q_s h}h\boldsymbol{q}_s\cdot\boldsymbol{F}_s. \tag{2.20}$$

In order to satisfy equation (2.6) we must choose

$$\check{G}_z(\boldsymbol{q}_s) = 2\mathrm{e}^{-q_s h}(\mathrm{i}h\boldsymbol{q}_s\cdot\boldsymbol{F}_s - (1+q_s h)F_z). \tag{2.21}$$

The surface velocity is entirely determined by the surface force $\tilde{f}_s$:

$$\check{\boldsymbol{u}}_s(\boldsymbol{q}_s) = \frac{q_s^2\boldsymbol{I}_s - \boldsymbol{q}_s\,\boldsymbol{q}_s}{(\eta_1+\eta_2)q_s^3(1+\mathscr{B}q_s a)}\cdot\check{\check{\boldsymbol{f}}}_s(\boldsymbol{q}_s). \tag{2.22}$$

Fourier transformation of equation (2.7) with $\boldsymbol{f}_s = 0$ leads to

$$\check{\check{\boldsymbol{f}}}_s(\boldsymbol{q}_s) = \mathrm{e}^{-q_s h}\left[\mathrm{i}q_s h\frac{\boldsymbol{q}_s\boldsymbol{e}_z}{q_s} + \boldsymbol{I}_s\right]\cdot\boldsymbol{F}. \tag{2.23}$$

Insertion of (2.18) and (2.23) into (2.19a) and inverse Fourier transformation leads to (Appendix A)

$$\boldsymbol{u}(x) = \int \mathrm{d}^3\boldsymbol{x}'\left[\boldsymbol{O}^M(\boldsymbol{x}_s-\boldsymbol{x}'_s, z, z') + \boldsymbol{O}^M_s(\boldsymbol{x}_s-\boldsymbol{x}'_s, z, z')\right]\cdot\boldsymbol{F}\delta^3(\boldsymbol{x}'-h\boldsymbol{e}_z), \tag{2.24}$$

where

$$\left.\begin{aligned}
\boldsymbol{O}^M(\boldsymbol{r}_s, z, h) &= \frac{\Theta(zh)}{8\pi\eta}\left\{o_{zz}\boldsymbol{e}_z\boldsymbol{e}_z + o_{zr}\frac{\boldsymbol{e}_z r_s}{r_s} + o_{rz}\frac{\boldsymbol{r}_s\boldsymbol{e}_z}{r_s} + o_{iso}\boldsymbol{I}_s + o_{aniso}\left[2\frac{\boldsymbol{r}_s r_s}{r_s^2} - \boldsymbol{I}_s\right]\right\},\\
\boldsymbol{O}^M_s(\boldsymbol{r}_s, z, h) &= \frac{1}{8\pi(\eta_1+\eta_2)}\left\{o^s_{iso}\boldsymbol{I}_s + o^s_{aniso}\left[2\frac{\boldsymbol{r}_s r_s}{r_s^2} - \boldsymbol{I}_s\right]\right\},
\end{aligned}\right\} \tag{2.25}$$

and

$$\left.\begin{aligned} o_{zz}(r_s,h,z) &= \left[\frac{1}{d_m}+\frac{(z-h)^2}{d_m^3}-\frac{1}{d_p}-\frac{z^2+h^2}{d_p^3}-\frac{6zh(z+h)^2}{d_p^5}\right],\\ o_{zr}(r_s,h,z) &= r_s\left[\frac{z-h}{d_m^3}-\frac{z-h}{d_p^3}+\frac{6zh(z+h)}{d_p^5}\right],\\ o_{rz}(r_s,h,z) &= r_s\left[\frac{z-h}{d_m^3}-\frac{z-h}{d_p^3}-\frac{6zh(z+h)}{d_p^5}\right],\\ o_{iso}(r_s,h,z) &= \left[\frac{3}{2d_m}-\frac{(z-h)^2}{2d_m^3}-\frac{3}{2d_p}+\frac{z^2+h^2+4zh}{2d_p^3}-\frac{3zh(z+h)^2}{d_p^5}\right],\\ o_{aniso}(r_s,h,z) &= \left[\frac{r_s^2}{2d_m^3}-\frac{r_s^2}{2d_p^3}+\frac{3zhr_s^2}{d_p^5}\right], \end{aligned}\right\} \tag{2.26a}$$

$$\left.\begin{aligned} o^s_{iso}(r_s,h,z) &= 2\int_0^\infty \mathrm{d}t\,\mathrm{e}^{-t}\frac{1}{\left(r_s^2+(|z|+|h|+\mathscr{B}at)^2\right)^{1/2}},\\ o^s_{aniso}(r_s,h,z) &= 2\int_0^\infty \mathrm{d}t\,\mathrm{e}^{-t}\frac{\left[\left(r_s^2+\left(|z|+|h|+\mathscr{B}at\right)^2\right)^{1/2}-\left(|z|+|h|+\mathscr{B}at\right)\right]^2}{r_s^2\left(r_s^2+(|z|+|h|+\mathscr{B}at)^2\right)^{1/2}}, \end{aligned}\right\} \tag{2.26b}$$

where

$$d_m=\sqrt{r_s^2+(z-h)^2},\quad d_p=\sqrt{r_s^2+(z+h)^2}, \tag{2.27}$$

with

$$\boldsymbol{r}_s=\boldsymbol{x}_s-\boldsymbol{x}'_s \tag{2.28}$$

a vector in the monolayer plane.

3. Flow around cylindrical symmetric obstacles

Let us now restrict attention to flow caused by cylindrical symmetrical obstacles. In these problems, the velocity and force field may be written as

$$\left.\begin{aligned} \boldsymbol{u}(x) &= U\left[u_0(x_s/a,z/a)\boldsymbol{e}_+ + \mathrm{e}^{\mathrm{i}\phi}u_1(x_s/a,z/a)\boldsymbol{e}_z + \mathrm{e}^{2\mathrm{i}\phi}u_2(x_s/a,z/a)\boldsymbol{e}_-\right],\\ \boldsymbol{f}(x') &= \frac{F}{a^2}\left[f_0(x'_s/a,h/a)\boldsymbol{e}_+ + \mathrm{e}^{\mathrm{i}\phi'}f_1(x'_s/a,h/a)\boldsymbol{e}_z + \mathrm{e}^{2\mathrm{i}\phi'}f_2(x'_s/a,h/a)\boldsymbol{e}_-\right], \end{aligned}\right\} \tag{3.1}$$

where $\boldsymbol{e}_\pm=(\boldsymbol{e}_x\pm\mathrm{i}\boldsymbol{e}_y)/\sqrt{2}$ and u_i, f_i, $i=0,1,2$ are the real components of the velocity and force in terms of the basis $\boldsymbol{e}_\pm$, $\boldsymbol{e}_z$. The velocity and force vectors are complex and we regain real vectors by adding or subtracting the complex conjugate solutions. Substituting $\gamma=\phi-\phi'$ we arrive at

$$\begin{pmatrix}u_0\\u_1\\u_2\end{pmatrix} = \int_{-\infty}^{\infty}\mathrm{d}h\int_0^\infty \mathrm{d}x'_s x'_s\int_{-\pi}^{\pi}\mathrm{d}\gamma\left[\boldsymbol{O}^M+\boldsymbol{O}_s^M\right]\cdot\begin{pmatrix}f_0\\f_1\\f_2\end{pmatrix} \tag{3.2}$$

where the components of Oseen's tensor in this basis are

$$8\pi\eta \boldsymbol{O}^M = \begin{pmatrix} o_{iso} & \frac{o_{rz}}{\sqrt{2}}\frac{x_s\cos\gamma - x_s'}{r_s} & o_{aniso}\left(1-\frac{2x_s^2\sin^2\gamma}{r_s^2}\right) \\ \frac{o_{zr}}{\sqrt{2}}\frac{x_s - x_s'\cos\gamma}{r_s} & o_{zz}\cos\gamma & \frac{o_{zr}}{\sqrt{2}}\frac{x_s\cos 2\gamma - x_s'\cos\gamma}{r_s} \\ o_{aniso}\left(1-\frac{2x_s'^2\sin^2\gamma}{r_s^2}\right) & \frac{o_{rz}}{\sqrt{2}}\frac{x_s\cos\gamma - x_s'\cos 2\gamma}{r_s} & o_{iso}\cos 2\gamma \end{pmatrix} \tag{3.3}$$

where

$$r_s = \sqrt{(x_s + x_s')^2 - 4x_s x_s'\cos^2\gamma/2}. \tag{3.4}$$

An equation similar to (3.3) holds for $\boldsymbol{O}_{\boldsymbol{s}}^M$. The integration over γ

$$\bar{\boldsymbol{O}}^M(x_s, z|x_s', h) := \int_{-\pi}^{\pi} \mathrm{d}\gamma\, \boldsymbol{O}^M \tag{3.5}$$

may be performed analytically and the rather lengthy result is tabulated in Appendix A.

We want to find the force profile that the object exerts on the fluid when it is moving with velocity $U\boldsymbol{e}_+$ and rotating around its centre z_c with angular frequency $-\mathrm{i}\Omega\boldsymbol{e}_+$. We find

$$\left.\begin{aligned} u_0 &= (U - \mathrm{i}\Omega(z(t) - z_c)) \\ u_1 &= \mathrm{i}\Omega\rho(t)/\sqrt{2} \\ u_2 &= 0 \end{aligned}\right\} \quad \text{for} \quad (x_s, z) \in \partial\boldsymbol{O}, \tag{3.6}$$

$$u_i(t) = \int_{t_{min}}^{t_{max}} \rho(t')\,\mathrm{d}s(t')\left[\bar{\boldsymbol{O}}_{ij}^M(\rho(t), z(t)|\rho(t'), z(t')) + \bar{\boldsymbol{O}}_{min}^M(\rho(t), z(t)|\rho(t'), z(t'))\right]\cdot f_j(t'), \tag{3.7}$$

where

$$\partial\boldsymbol{O} := \{x_s, z| \quad \text{with} \quad x_s = \rho(t),\ z = z(t), \qquad t_{min} < t < t_{max}\} \tag{3.8}$$

is an arbitrarily chosen parametrization of the contour of the cylindrical symmetric surface $\partial\boldsymbol{O}$ of the object and

$$\mathrm{d}s(t') = \sqrt{(\mathrm{d}\rho/\mathrm{d}t')^2 + (\mathrm{d}z/\mathrm{d}t')^2}\,\mathrm{d}t' \tag{3.9}$$

is the arclength increment corresponding to the parametrization. Equations (3.6) and (3.7) define a one-dimensional integral equation on $\partial\boldsymbol{O}$ for the three unknown components of the force profile on the surface of the sphere. It can be solved numerically, by discretizing the integral, which converts the integral equation into a matrix equation (Appendix B). Inversion of the matrix then yields the force profile. The drag force $F^{drag}\boldsymbol{e}_+$ is then given by

$$F^{drag} = \int_{t_{min}}^{t_{max}} 2\pi\rho(t')\,\mathrm{d}s(t')\,f_0(t') \tag{3.10}$$

and the drag torque $-\mathrm{i}T^{drag}\boldsymbol{e}_+$ equals†

$$T^{drag} = \int_{t_{min}}^{t_{max}} 2\pi\rho(t')\,\mathrm{d}s(t')\,[(z(t') - z_c)\,f_0(t') - \rho(t')\,f_1(t')/\sqrt{2}]. \tag{3.11}$$

The drag force and torque are connected to the velocity U and angular frequency Ω via

$$\begin{pmatrix} \dfrac{F^{drag}}{\eta_1 a^2} \\ \dfrac{T^{drag}}{\eta_1 a^3} \end{pmatrix} = \begin{pmatrix} k_T & k_C \\ k_C & k_R \end{pmatrix} \cdot \begin{pmatrix} \dfrac{U}{a} \\ \Omega \end{pmatrix}. \tag{3.12}$$

Numerically solving the integral equation (3.7) for $\Omega = 0$ yields the coefficients k_T and k_C, while setting $U = 0$ yields the force profile for the rotational coefficients.

4. Results and discussion

4.1. *large Boussinesq number*

For high surface shear viscosity, the components of the surface Oseen tensor simplify and we find (Appendix A)

$$\left.\begin{aligned} \lim_{\mathscr{B}\to\infty} \bar{o}^M_{s00} &= \frac{4\pi}{\mathscr{B}a}\left(\ln\frac{2\mathscr{B}a}{|z| + |h| + \sqrt{(x_s + x_s')^2 + (|z| + |h|)^2}} - \gamma\right) + o(1/\mathscr{B}), \\ \lim_{\mathscr{B}\to\infty} \bar{o}^M_{s22} &= \lim_{\mathscr{B}\to\infty} \bar{o}^M_{s02} = o(1/\mathscr{B}^2), \end{aligned}\right\}. \tag{4.1}$$

If the object is immersed in the interface, the integral equation (3.7) is solved by a force density profile that is concentrated at the interface:

$$\left.\begin{aligned} \lim_{\mathscr{B}\to\infty} f_0(h) &= 2(\eta_1 + \eta_2)aU\delta(h)\frac{\mathscr{B}}{\ln \mathscr{B}a/a_s - \gamma} + o(\mathscr{B}^0), \\ \lim_{\mathscr{B}\to\infty} f_1 &= \lim_{\mathscr{B}\to\infty} f_1 = o(\mathscr{B}^0), \end{aligned}\right\} \tag{4.2}$$

where $a_s = \rho(0)$ defines the radius of the cylindrical symmetric object at the interface. The drag force is given by

$$\lim_{\mathscr{B}\to\infty} F_{drag} = 4\pi(\eta_1 + \eta_2)aU\frac{\mathscr{B}}{\ln \mathscr{B}a/a_s - \gamma}. \tag{4.3}$$

If the object is a sphere of radius a then $a_s/a = \sin\Theta$ with Θ the contact angle of the liquid interface with the sphere.

4.2. *Filaments*

The result (4.3) holds for any object that protrudes into the surface with a protrusion of depth l that is of the order of the interfacial radius a_s. It differs only slightly from the result of Saffmann & Delbrück (1975) derived for non-protruding objects.‡

† All quantities, F^{drag}, U, $-\mathrm{i}T^{drag}$, and $-\mathrm{i}\Omega$ are understood as coordinates with respect to the basis vector $\boldsymbol{e}_+$. The coupling coefficients are real and the factor $-\mathrm{i}$ in front of the angular velocity and torque indicate that they point in a direction rotated by $\pi/2$ around the z-axis with respect to the direction of the force and the velocity.

‡ Equation (4.3) differs from Saffman & Delbrück's original result in that in the denominator $\ln(2\mathscr{B})$ is replaced by $\ln(\mathscr{B}\sin\theta)$, the factor 2 in the logarithm of Saffman & Delbrück's result arises since there the entire disk is immersed into the interface, while our result holds for objects with only the rim of radius a_s cutting the surface.

If an object protrudes much further into the subphase ($l \gg a$) the force density on the surface of the object in the subphase, although of $o(\mathscr{B}'^0)$, might add up to a comparable total drag when integrated over the comparably long protrusion. The geometry considered in this subsection therefore is that of an elongated highly anisotropic polymer or filament protruding normal to the membrane into one of the bulk phases and touching the membrane with one of its ends. The requirement of large protrusion is fulfilled if we have $a \ll l$, where a is the radius of the filament, l its length and $\mathscr{B}' = \eta_s/\eta a$ the Boussinesq number defined in terms of the radius of the filament. As in the previous section we exclusively consider high Boussinesq numbers $\mathscr{B}' \gg 1$. An experimentally relevant example of such a configuration is microvilli. Microvilli are short or long finger-like extensions from the cell surface that are responsible for the dynamic assembly of sceletal infrastructure of the cell membrane as well as for the membrane motion on the microscopic scale. The core of the microvilli is made up of a group of actin microfilaments which interdigitate with a band of microfilaments just below the cell membrane. These microfilaments are about 3–6 nm in diameter (Mercier *et al.* 1989). They not only provide a sceletal core to maintain the structure of the microvilli but they are also believed to be responsible for providing a mechanism for passage of nutrients across the cell membrane when they interact with the myosin. The drag on filaments is important when calculating the power consumption required for a short-range diffusive motion of such microvilli (Manneville *et al.* 2003). However, the hydrodynamic derivation given here is more general and also applies to other realization of this geometry such as the motion of nano-rods or rigid fibres in a membrane or a monolayer.

In the limit of vanishing radius of the filament only the 00-component of the Oseen tensor is relevant. The parametrization of the filament is given by $\rho(z) = a \to 0$ and the Oseen tensor component simplifies to

$$\lim_{a\to 0} \bar{o}^M_{00} = \begin{cases} 0 & \text{if } z = 0, \\ 8\pi \ln(l/2a)\delta(z-h) & \text{if } z, h > a, \end{cases} \tag{4.4a}$$

$$\lim_{a\to 0} \bar{o}^M_{s00} = \begin{cases} \dfrac{4\pi}{\mathscr{B}'a}(\ln \mathscr{B}' - \gamma) & \text{if } z = 0 \\ -\dfrac{32\pi}{\mathscr{B}'a} \exp\left(\dfrac{z+h}{\mathscr{B}'a}\right) \mathrm{Ei}\left(-\dfrac{z+h}{\mathscr{B}'a}\right) & \text{if } z + h > a, \end{cases} \tag{4.4b}$$

where $\mathrm{Ei}(x)$ is the exponential integral function. The integral equation (3.7) is then solved by

$$f_0(h) = 2(\eta_1 + \eta_2)aU\delta(h)\frac{\mathscr{B}'}{\ln \mathscr{B}' - \gamma} + \frac{\eta_1 U}{\ln l/2a}\left(1 - 8\frac{\mathrm{e}^{h/\mathscr{B}'a}\mathrm{Ei}(-h/\mathscr{B}'a)}{\ln \mathscr{B}' - \gamma}\right). \tag{4.5}$$

The drag force is obtained using (3.10):

$$\begin{aligned} k_T &= \frac{F^{drag}}{(\eta_1+\eta_2)aU} \\ &= \left(\frac{4\pi\mathscr{B}'}{\ln \mathscr{B}' - \gamma} + \frac{2\pi\eta_1\mathscr{B}'}{(\eta_1+\eta_2)\ln(l/2a)}\left(\frac{l}{a\mathscr{B}'} + 8\frac{\ln(l/\mathscr{B}'a) + \gamma - \mathrm{e}^{l/\mathscr{B}'a}\mathrm{Ei}(-l/\mathscr{B}'a)}{\ln \mathscr{B}' - \gamma}\right)\right). \end{aligned} \tag{4.6}$$

Figure 2 shows equation (4.6) for a filament attached to a monolayer ($\eta_2 = 0$) as a function of the Boussinesq number. There is a crossover from a drag strongly depending on the aspect ratio l/a but almost independent of $\mathscr{B}'$ at low Boussinesq numbers toward a drag strongly depending on the Boussinesq number $\mathscr{B}'$ but

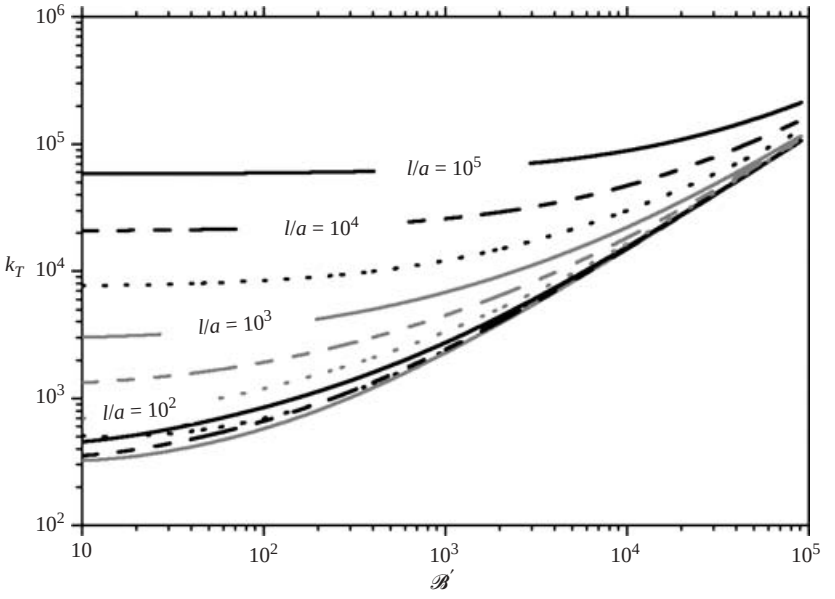

FIGURE 2. Numerical solution for the drag coefficients of a filament piercing a monolayer ($\eta_2 = 0$) as a function of the Boussinesq number $\mathscr{B}'$ for different aspect ratios l/a of the filament.

independent of the aspect ratio l/a at high Boussinesq number. The drag force becomes protrusion dominated for $l/a > \mathscr{B}'$ and is dominated by the surface viscosity in the opposite case. The crossover from protrusion dominated to surface viscosity dominated drag occurs at the knee of the curves that is located roughly at $\mathscr{B}' \approx l/a$.

4.3. *Spheres*

Let us now consider the problem of a sphere of radius a immersed in the flat interface with its north pole at a distance d from the interface. We parametrize the surface of the sphere as

$$\left.\begin{aligned} &\partial S := \{x_s', h \big| \quad \text{with} \quad x_s' = \rho(h) \qquad z_{min} < h < z_{max}\}, \\ &\rho(h) = \sqrt{a^2 - (h - z_c)^2}, \end{aligned}\right\} \tag{4.7}$$

where

$$z_{min} = d, \qquad z_c = d + a, \qquad z_{max} = d + 2a \tag{4.8}$$

and

$$\rho(h)\,\mathrm{d}s(h) = a\,\mathrm{d}h. \tag{4.9}$$

The inversion of (3.7) is well-behaved for the f_0-component and for the f_1-component if none of the poles of the sphere touches the surface ($d \not\approx -2a$ and $d \not\approx 0$). If the sphere touches the monolayer (membrane), the force profile of the rotational problem $U = 0$ exhibits a singularity in the f_1-component near the contact line (O'Neill *et al.* 1986; Huh & Scriven 1971; Dussan V. & Davis 1974):

$$f_1(h \to 0) = \frac{\boldsymbol{\tau}}{h}. \tag{4.10}$$

This singularity arises since the no slip condition cannot be sustained close to the three-phase contact line. It leads to a logarithmic singularity of the torque. We do

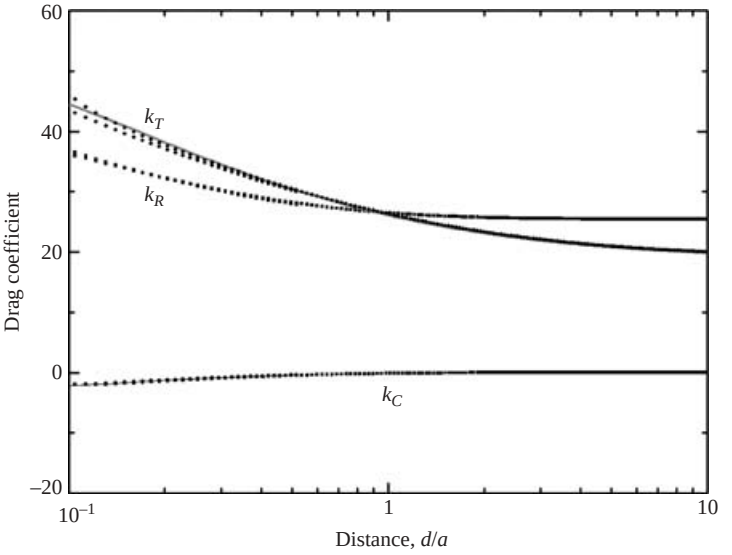

FIGURE 3. Numerical solution for the drag coefficients (black dots) as a function of the distance of the north pole from the interface for infinite Boussinesq number. The grey lines are fits to the numerics according to Faxen (1923).

not remove the singularity and therefore obtain $k_R = \infty$ as soon as the sphere touches the interface. The results for a sphere immersed in the interface at high Boussinesq numbers follows from the discussion in § 4.1.

4.4. *Sphere fully immersed in the subphase adjacent to a large-Boussinesq-number interface*

If the sphere is not immersed in the interface and the Boussinesq number is large, then we can neglect the surface Oseen tensor and we are left with the Oseen tensor of a rigid interface. Hence we recover the results for a sphere moving close to a solid wall (Faxen 1923). Figure 3 displays the translational, rotational and coupling drag coefficients obtained from our numerics. The solid lines are the analytical solutions by Faxen (1923) obtained with the method of reflections. The numerics reproduces Faxen's results.

4.5. *Low Boussinesq number*

For small Boussinesq number we expand both the surface Oseen tensor and the force density into a series in the Boussinesq number:

$$\left.\begin{aligned} \boldsymbol{O}^M &= \boldsymbol{O}^{M(0)} + \mathscr{B}\boldsymbol{O}^{M(1)} + o(\mathscr{B}^2), \\ \boldsymbol{f} &= \boldsymbol{f}^{(0)} + \mathscr{B}\boldsymbol{f}^{(1)} + o(\mathscr{B}^2). \end{aligned}\right\} \tag{4.11}$$

Sorting equation (3.2) into different orders in the Boussinesq number we obtain

$$\boldsymbol{u} = \int \boldsymbol{O}^{M(0)} \cdot \boldsymbol{f}^{(0)}, \tag{4.12a}$$

$$-\int \boldsymbol{O}^{M(1)} \cdot \boldsymbol{f}^{(0)} = \int \boldsymbol{O}^{M(0)} \cdot \boldsymbol{f}^{(1)}. \tag{4.12b}$$

By successively inverting the series of equations (4.12) we obtain the coefficients in the series in $\mathscr{B}$ of the force (4.11) and hence a series in $\mathscr{B}$ for the friction coefficients.

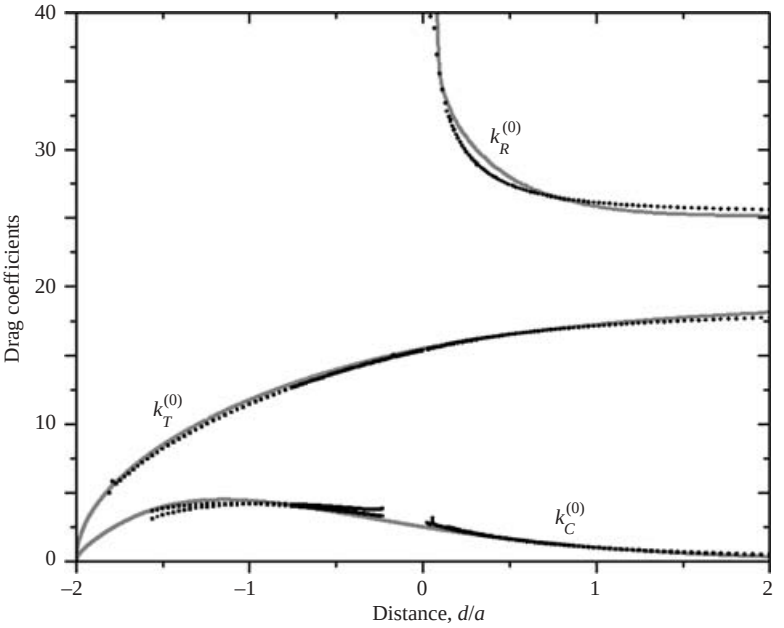

FIGURE 4. Numerical solution for the drag coefficients (black dots) as a function of the distance of the north pole from the monolayer surface for zero Boussinesq number. The grey lines are fits to the numerics according to equations (4.13). The coupling coefficieents do not converge near $d \approx 0$ and $d \approx -2a$, since the series expansion in the Boussinesq number of Oseen's tensor no longer converges for $\mathscr{B} \to 0$. No numerical data are shown in these regimes.

The radius of convergence of the series of the force shrinks to zero with the radius of the three-phase intersection line. For a disk lying flat in the interface a convergent series with logarithmic corrections incorporated exists; however the power series diverges. In the following sections we numerically compute the solutions to the drag coefficients in linear order of the Boussinesq number ($k = k^{(0)} + \mathscr{B}k^{(1)} + o(\mathscr{B}^2)$) avoiding immersion depths of the sphere where the north or south pole touches the interface.

4.6. *Sphere in a monolayer*

Figure 4 shows the numerical result for the drag coefficients $k_T^{(0)}$, $k_C^{(0)}$, and $k_R^{(0)}$ for zero Boussinesq number as a function of the immersion depth of the bead in a non-viscous ($\eta_s = 0$) monolayer on a liquid (η_1)/air ($\eta_2 = 0$) interface. The translational, rotational and coupling drag are fitted with an accuracy of 3% by the formula

$$k_T^{(0)} \approx 6\pi\sqrt{\tanh[32(d/a+2)/(9\pi^2)]}, \tag{4.13a}$$

$$k_R^{(0)} \approx \begin{cases} 8\pi - 5\ln(\tanh(3d/2a)) & \text{for } d > 0 \\ \infty & \text{for } d \leqslant 0, \end{cases} \tag{4.13b}$$

$$k_C^{(0)} \approx \left(4(d/a+2)^{1/2} + 16(d/a+2)^{3/2}\right) \mathrm{e}^{-3(d+2a)/2a}. \tag{4.13c}$$

All drag coefficients approach their correct theoretical values $k_T = 6\pi$, $k_C = 0$, and $k_R = 8\pi$ when the sphere is far away from the surface ($d \to \infty$) (Happel & Brenner 1983). For $d \to -2a$ the translational and coupling drag coincides with that of a disk of radius $a_D = \sqrt{2a(d+2a)}$ immersed in a monolayer (Hughes *et al.* 1981).

The translational drag monotonically increases with the immersion depth of the sphere. Both coupling coefficients are positive and equal within the error margins of the numerics. A torque-free sphere will hence rotate in the opposite sense, as if the

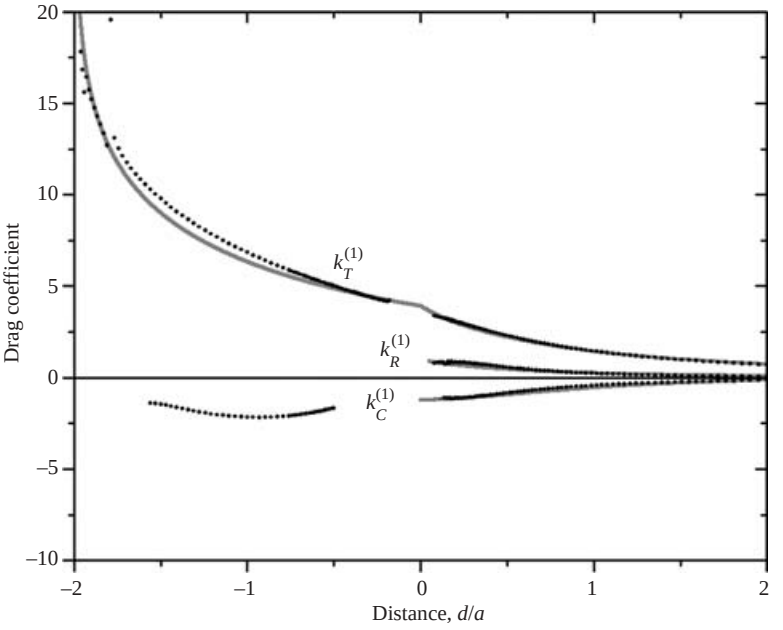

FIGURE 5. Numerical solution for the first-order correction to the drag coefficients (black dots) as a function of the distance of the north pole from the monolayer surface. The grey lines are fits to the numerics according to equations (4.14). The coupling coefficients do not converge near $d \approx 0$ and $d \approx -2a$, since the series expansion in the Boussinesq number of Oseen's tensor no longer converges for $\mathscr{B} \to 0$. No numerical data are shown in these regimes.

sphere were rolling on the monolayer surface. No discontinuity is observed in the translational and coupling drag when the sphere detaches from the monolayer surface as it is fully immersed in the liquid. However, the rotational drag logarithmically diverges. Because of the divergence of the rotational drag in spite of the asymmetry of the problem, a torque-free sphere will hardly rotate when one applies a force to one in contact with the monolayer.

Figure 5 shows the numerical result for the first-order correction of the drag coefficients $k_T^{(1)}$, $k_C^{(1)}$ and $k_R^{(1)}$ as a function of the immersion depth of the sphere. The translational, rotational and coupling drag is fitted with an accuracy of 3% by the formula

$$k_T^{(1)} \approx \begin{cases} -4 \ln\left(\frac{2}{\pi} \arctan\left(\frac{2}{3}\right)\right) \frac{a^{3/2}}{(d+3a)^{3/2}} & \text{for } d > 0 \\ -4 \ln\left(\frac{2}{\pi} \arctan\left(\frac{d+2a}{3a}\right)\right) & \text{for } d < 0, \end{cases} \tag{4.14a}$$

$$k_R^{(1)} \approx \begin{cases} \frac{a^2}{(d+a)^2} & \text{for } d > 0 \\ \infty & \text{for } d < 0, \end{cases} \tag{4.14b}$$

$$k_C^{(1)} \approx -\frac{1.2}{\cosh(3d/2a)} \qquad \text{for } d > 0. \tag{4.14c}$$

All drag coefficient corrections vanish when the sphere is far away from the surface ($d \to \infty$) (Happel & Brenner 1983). The corrections $k_T^{(1)}$ and $k_R^{(1)}$ are both positive, indicating that the surface shear viscosity increases both the translational and rotational drag. The correction to the coupling coefficient is negative and of opposite sign to the leading term. When on a non-viscous surface the sphere would prefer

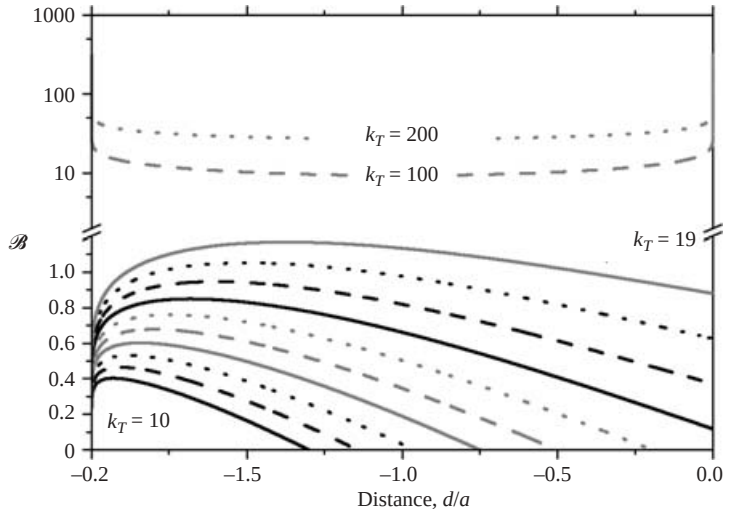

FIGURE 6. Iso-translational-friction lines in the $(d, \mathscr{B})$-plane for $k_T = 10, 11, ...19, 100, 200$. An experiment revealing a friction coefficient of 16 can be interpreted to result (*a*) from an immersion of the sphere or (*b*) from surface viscous contributions.

to rotate in the opposite direction as if rolling on the monolayer; the viscous contribution of the monolayer supports rotation in the same sense as if rolling on the surface. The translational drag monotonically increases with the immersion depth of the sphere. Both coupling coefficients are equal within the error margins of the numerics. No discontinuity is observed in the translational and coupling drag when the sphere detaches from the monolayer surface as it is fully immersed in the liquid. However, the rotational drag logarithmically diverges. Because of the divergence of the rotational drag in spite of the asymmetry of the problem, a torque-free sphere will hardly rotate when one applies a force to one in contact with the monolayer.

The translational drag on a half-immersed sphere $k_T^{(0)} \approx 11.7$ in a non-viscous monolayer is about 25% larger than the drag on a non-rotating sphere immersed in a free surface $k_T = 3\pi$. This is in excellent agreement with the estimate by Stone (2005, personal communication) using a perturbative expansion in the protrusion. The incompressibility (equation (2.5)) leads to corrections to the drag on a free surface (Danov *et al.* 1995, 2000) that are similar in magnitude to experimentally observed deviations (Petkov *et al.* 1995; Sickert & Rondelez 2003, 2004) which have been attributed to surface viscous damping and viscosity of water that was renormalized by 30%. A variation in immersion depth, and a variation of drag caused by the Marangoni effect, however, are alternative sources of drag increase that cannot be easily ruled out in the experiments. Such variations in depth have been predicted to arise due to electrocapillary effects for micron-sized spheres by Nikolaides *et al.* (2002). Electrocapillary effects have been confirmed by Danov *et al.* (2004) by measurements on large (100 micrometer sized) beads. Electrocapillary effects are predicted to be most pronounced for small spheres with diameter at or below the microscopic resolution limit. Our calculations, although neglecting the deformation of the surface caused by the electrocapillary effects, can be an indirect way of determining the effective immersion of spheres in the interface from the increase or decrease in mobility with respect to the mobility of a sphere immersed at its contact angle in a flat interface. In figure 6 we plot lines of equal friction for spheres immersed in a viscous monolayer in the $(d, \mathscr{B})$-plane. As can be seen, a translational friction constant of $k_T = 15$ as measured on the

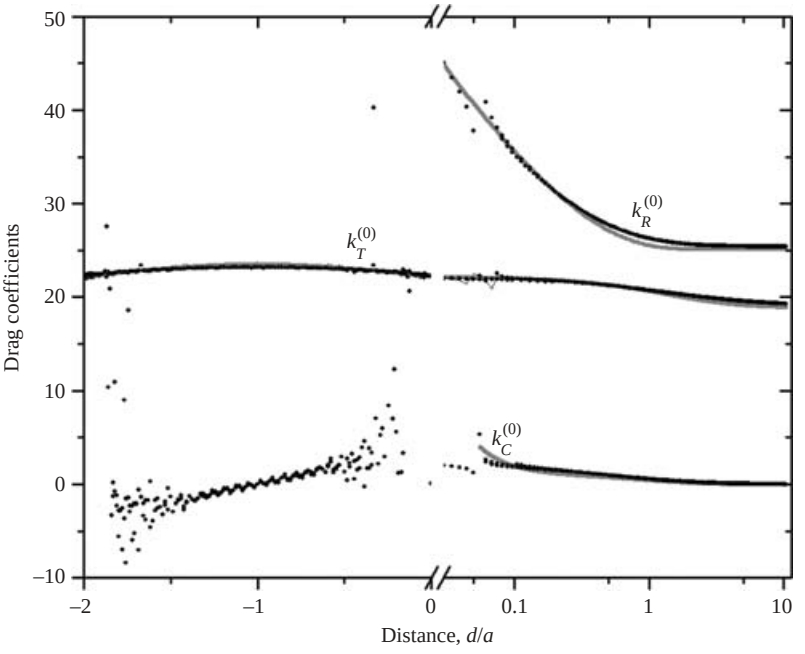

FIGURE 7. Numerical solution for the drag coefficients (black dots) as a function of the distance of the north pole from the membrane surface for zero Boussinesq number. The grey lines are fits to the numerics according to equation (4.15). The coupling coefficients do not converge near $d \approx 0$, since the series expansion in the Boussinesq number of Oseen's tensor no longer converges for $\mathscr{B} \to 0$. The data are displayed on a linear scale for the immersion depths when the sphere touches the membrane and on a logarithmic scale when the sphere is fully immersed in one of the phases.

simple air–water interface by Sickert & Rondelez (2003, 2004) is compatible with a deeply immersed sphere $d \approx -0.25a$ on an impure and therefore incompressible surface. No renormalization of the viscosity of water is necessary to explain their observation. On discarding the viscosity renormalization and using our theory with the proper viscosity of water the measurements of the diffusion of colloidal beads in various monolayers of Sickert & Rondelez (2003, 2004) are explained with surface shear viscosities of $\eta_s \approx 0.3 \times 10^{-9}\,\mathrm{N\,s\,m^{-1}}$ which is the same order of magnitude as Sickert & Rondelez (2003, 2004), found using a renormalized bulk viscosity.

4.7. *Sphere in a membrane*

Figure 7 shows the numerical result for the drag coefficients $k_T^{(0)}$, $k_C^{(0)}$, and $k_R^{(0)}$ for zero Boussinesq number as a function of the immersion depth of the bead in a non-viscous ($\eta_s = 0$) membrane between two liquids of similar viscosity ($\eta_1 = \eta_2$). The data are displayed on a linear scale for the immersion depths when the sphere touches the membrane and on a logarithmic scale when the sphere is fully immersed in one of the phases.

The translational, rotational and coupling drag is fitted with an accuracy of 3% by the formula

$$k_T^{(0)} \approx 6\pi + \frac{3\pi/2}{1+(d/a+1)^2}, \tag{4.15a}$$

$$k_R^{(0)} \approx \begin{cases} 8\pi + 3|\ln(\tanh(d/a))|^{3/2} & \text{for } d > 0 \\ \infty & \text{for } d < 0, \end{cases} \tag{4.15b}$$

$$k_C^{(0)} \approx \pi \mathrm{e}^{-(d/a+1)} + 0.009a^2/d^2. \tag{4.15c}$$

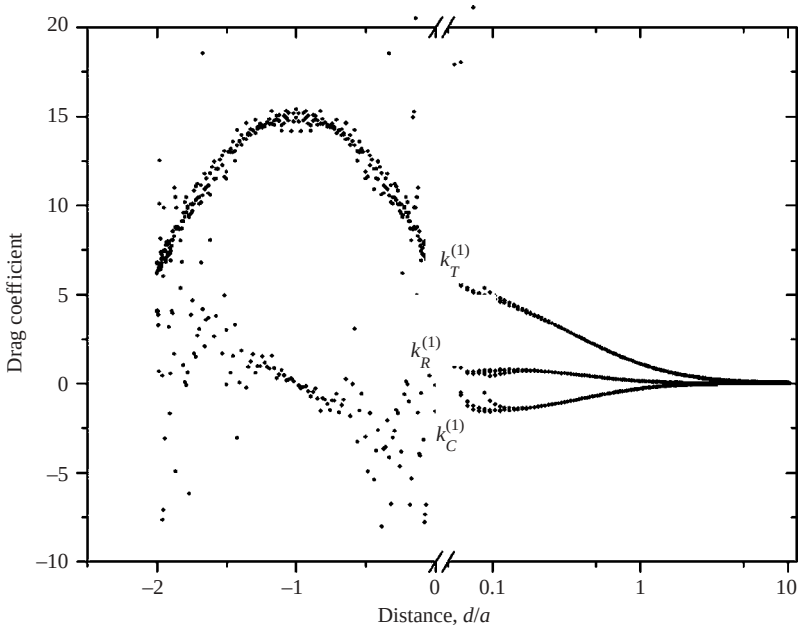

FIGURE 8. Numerical solution for the first-order corrections to the drag coefficients (black dots) as a function of the distance of the north pole from the membrane surface. The coupling coefficients do not converge near $d \approx 0$, since the series expansion in the Boussinesq number of Oseen's tensor no longer converges for $\mathscr{B} \to 0$. The data are displayed on a linear scale for the immersion depths when the sphere touches the membrane and on a logarithmic scale when the sphere is fully immersed in one of the phases.

All drag coefficients approach their correct theoretical values $k_T = 6\pi$, $k_C = 0$, and $k_R = 8\pi$ when the sphere is far away from the surface ($d \to \infty$) (Happel & Brenner 1983).

The translational drag is maximal when the sphere is symmetrically immersed in both phases with the equator coinciding with the membrane plane. The drag monotonically decreases when moving to either side. The two coupling coefficients are equal within the error margins of the numerics. No discontinuity is observed in the translational drag when the sphere detaches from the membrane surface as it is fully immersed in one liquid. However, the rotational drag logarithmically diverges. The translational drag on a half-immersed sphere $k_T^{(0)} \approx 15\pi/2$ is 25% larger than the drag on a non-rotating sphere immersed in a free surface $k_T^{(0)} = 6\pi$. The incompressibility (equation (2.5)) leads to corrections to the drag on a free surface (Danov *et al.* 1995, 2000) that are similar in magnitude to experimentally observed deviations (Dimova *et al.* 1999*a*, *b*, 2000) which have been attributed to surface viscous damping. A variation in immersion depth, and a variation of drag caused by the Marangoni effect, however, are alternative sources of drag increase that cannot be easily ruled out in the experiments.

Figure 8 shows the numerical result for the first-order corrections to the Boussinesq number of the drag coefficients $k_T^{(1)}$, $k_C^{(1)}$, and $k_R^{(1)}$ as a function of the immersion depth of the bead in a membrane between two liquids of similar viscosity ($\eta_1 = \eta_2$). The data are displayed on a linear scale for the immersion depths when the sphere touches the membrane and on a logarithmic scale when the sphere is fully immersed in one of the phases.

The translational first-order correction $k_T^{(1)}$ exhibits a maximum when the sphere is positioned with its equator in the membrane. It continuously changes as the sphere detaches from the membrane and drops to zero when it is far away from the membrane. The first-order correction to the rotational drag $k_R^{(1)}$ is rather weak when compared with the leading order and a slightly viscous membrane does not change the rotational torque. The first-order coupling correction $k_C^{(1)}$ acts opposite to the leading order because the viscous membrane exerts a force that rolls the sphere on the membrane, while in the non-viscous case the sphere tends to roll on the bulk phase into which the sphere protrudes more.

It is clear from the calculations that a fully immersed sphere with $0 < d \ll a$, rigidly coupled to a flat solid disk (*raft*) of radius $a_D \ll a$ will not experience a translational drag significantly different to that of a sphere touching the monolayer with its north pole $d \approx 0$. It will not be possible to use a sphere with radius much bigger than the disk (raft) to detect the hydrodynamic radius of the disk. The hydrodynamic radius of *lipid rafts* found in Pralle *et al.* (2000) is presumably much larger than their estimate. It is therefore necessary to calculate the drag on spheres in or close to a membrane/monolayer analytically. Here we have done this for a viscous monolayer coupled to an infinitely deep subphase on one side of the monolayer and for a viscous membrane with the same viscous liquid on both sides of the membrane.

5. Conclusions

The drag on a sphere immersed and moving in an incompressible viscous monolayer on a viscous infinitely deep subphase is calculated numerically. On a membrane or monolayer of low viscosity the viscous drag is larger than on a free surface. A small protrusion of the object alters the drag at low surface shear viscosities. At high viscosities effects of protrusion are only relevant if the protrusion is larger than $l > \eta_s/(\eta_1 + \eta_2)$ which applies for objects like filaments or nano-rods. Simple analytical expressions for the drag coefficients are given in various limiting cases for spheres and for filaments, which coincide with the numerical result within 3%. In a monolayer the drag increases monotonically with the depth of immersion of the sphere. Rotation of the sphere can be neglected when the size of the sphere is large compared to the thickness of the monolayer and when the sphere touches the monolayer. No discontinuity of the drag arises when the sphere is totally immersed in the subphase and detaches from the monolayer. The drag in a membrane decreases as the sphere is displaced out of its equatorial position. The Marangoni effect is an essential feature for the analysis of surface viscous properties using colloidal particle tracking techniques. Applying our numerical derivations to experiments of Sickert & Rondelez (2003, 2004) results in similar surface shear as derived in their work; however the results are achieved without unphysical renormalization of the bulk viscosity. Experimental results of Sickert & Rondelez (2003, 2004) on the diffusion of colloidal particles on bare but impure air/water interfaces that could not be explained with the theory of Danov *et al.* (1995, 2000) are explained within the framework of our theory. The hydrodynamic radii of membraneous domains measured by the drag of domain-coupled spheres are orders of magnitude larger than anticipated in the work of Pralle *et al.* (2000). Our calculations can be used for the measurement of electrocapillary immersion forces on spheres in a monolayer.

We thank Howard Stone for sharing his calculation on the mobility of protruding ellipsoids.

Appendix A. Oseen tensor in direct space

Here we outline the inverse Fourier transform leading to Oseen's tensor in direct space (equations (2.25) and (2.26)) and the angular integrals leading to the Oseen tensor for axial symmetric objects (equations (3.5) and (A 15)–(A 20)). The inverse Fourier transform is performed in cylindrical coordinates:

$$\boldsymbol{O}^M(\boldsymbol{r}) = \frac{1}{(2\pi)^3}\int_0^\infty q_s\,\mathrm{d}q_s\int_{-\pi}^{\pi}\mathrm{d}\psi\int_{-\infty}^{\infty}\mathrm{d}q_z \mathrm{e}^{-\mathrm{i}q_z z-\mathrm{i}q_s r_s\cos(\psi)}\hat{\boldsymbol{O}}^M(\boldsymbol{q}) \tag{A 1}$$

where we have writen equation (2.19) as

$$\hat{\boldsymbol{u}}(\boldsymbol{q}) = \hat{\boldsymbol{O}}^M(\boldsymbol{q})\cdot\boldsymbol{F}. \tag{A 2}$$

The explicit expression for $\hat{\boldsymbol{O}}^M(\boldsymbol{q})$ satisfying the boundary conditions (2.5)–(2.7) and (2.9) is obtained after insertion of equations (2.18), (2.21) and (2.23) into (2.19). The expression $(1+\mathscr{B}q_s a)^{-1}$ in the surface Oseen tensor is rewritten as

$$\hat{\boldsymbol{T}}_B(\boldsymbol{q}) = (1+\mathscr{B}q_s a)^{-1} = \int_0^\infty \mathrm{d}t\,\mathrm{e}^{-t}\mathrm{e}^{-\mathscr{B}q_s a t}. \tag{A 3}$$

The integration over q_z involves integrals of the type:

$$\frac{1}{2\pi}\int_{-\infty}^{\infty}\mathrm{d}q_z\mathrm{e}^{-\mathrm{i}q_z z}\frac{1}{q_z^2+q_s^2} = 2\frac{\mathrm{e}^{-q_s z}}{4q_s}, \tag{A 4a}$$

$$\frac{1}{2\pi}\int_{-\infty}^{\infty}\mathrm{d}q_z\mathrm{e}^{-\mathrm{i}q_z z}\frac{q_z}{q_z^2+q_s^2} = -2\mathrm{i}q_z\frac{\mathrm{e}^{-q_s z}}{4q_s}, \tag{A 4b}$$

$$\frac{1}{2\pi}\int_{-\infty}^{\infty}\mathrm{d}q_z\mathrm{e}^{-\mathrm{i}q_z z}\frac{1}{\left(q_z^2+q_s^2\right)^2} = \frac{1+q_s z}{q_s^2}\frac{\mathrm{e}^{-q_s z}}{4q_s}, \tag{A 4c}$$

$$\frac{1}{2\pi}\int_{-\infty}^{\infty}\mathrm{d}q_z\mathrm{e}^{-\mathrm{i}q_z z}\frac{q_z}{\left(q_z^2+q_s^2\right)^2} = -\mathrm{i}z\frac{\mathrm{e}^{-q_s z}}{4q_s}, \tag{A 4d}$$

$$\frac{1}{2\pi}\int_{-\infty}^{\infty}\mathrm{d}q_z\mathrm{e}^{-\mathrm{i}q_z z}\frac{q_z^2}{\left(q_z^2+q_s^2\right)^2} = (1-q_s z)\frac{\mathrm{e}^{-q_s z}}{4q_s}. \tag{A 4e}$$

From (A 3) and the first line of (A 4) we see that multiplication with $\hat{\boldsymbol{T}}_B(\boldsymbol{q})$ in Fourier space translates into a linear operator:

$$\begin{aligned}\boldsymbol{O}_s^M(\boldsymbol{r}_s, |z|+|h|, \mathscr{B}) &= \boldsymbol{T}_B\left\{\boldsymbol{O}_s^M(\boldsymbol{r}_s, |z|+|h|, \mathscr{B}=0)\right\}\\ &= \int_0^\infty \mathrm{d}t\,\mathrm{e}^{-t}\boldsymbol{O}_s^M(\boldsymbol{r}_s, |z|+|h|+\mathscr{B}at, \mathscr{B}=0)\end{aligned} \tag{A 5}$$

in real space. If $\boldsymbol{O}_s^M(\boldsymbol{r}_s, |z|+|h|+\mathscr{B}at, \mathscr{B}=0)$ is a function that may be expanded in a Taylor series in its second argument around $|z|+|h|$ we find that

$$\boldsymbol{T}_B = \sum_{n=0}^{\infty}\left(\mathscr{B}a\frac{\partial}{\partial|z|}\right)^n. \tag{A 6}$$

The integration over the polar angle involves integrals of the form

$$\frac{1}{(2\pi)^2}\int_{-\pi}^{\pi}\mathrm{d}\psi\mathrm{e}^{-\mathrm{i}q_s r_s\cos\psi} = \frac{1}{2\pi}J_0(q_s r_s), \tag{A 7a}$$

$$\frac{1}{(2\pi)^2}\int_{-\pi}^{\pi}\mathrm{d}\psi\mathrm{e}^{-\mathrm{i}q_s r_s\cos\psi}\frac{\boldsymbol{q}_s}{q_s} = \frac{-\mathrm{i}}{2\pi}J_1(q_s r_s)\frac{\boldsymbol{r}_s}{r_s}, \tag{A 7b}$$

$$\frac{1}{(2\pi)^2}\int_{-\pi}^{\pi} \mathrm{d}\psi \mathrm{e}^{-\mathrm{i}q_s r_s \cos\psi}\frac{\boldsymbol{q}_s\boldsymbol{q}_s}{q_s^2} = \frac{1}{2\pi}J_0(q_s r_s)\frac{\boldsymbol{r}\boldsymbol{r}}{r^2} + \frac{1}{2\pi}\frac{J_1(q_s r_s)}{q_s r_s}\left[\boldsymbol{I}_s - 2\frac{\boldsymbol{r}_s\boldsymbol{r}_s}{r_s^2}\right], \quad (A\,7c)$$

where $J_n(q_s r_s)$ are Bessel functions of the first kind of order n, and the integral over the lateral component of the $\boldsymbol{q}$-vector leads to integrals of the form

$$I_\nu^m := \int_0^\infty \mathrm{d}q_s q_s^{m-1}\mathrm{e}^{-q_s\zeta}J_\nu(q_s r_s) = \frac{(-1)^m}{\nu r_s^\nu}\frac{\mathrm{d}^m}{\mathrm{d}\zeta^m}\left(\sqrt{\zeta^2+r_s^2}-\zeta\right)^\nu. \quad (A\,8)$$

Specifically one finds

$$\left.\begin{aligned} I_0^1 &= \frac{1}{\sqrt{\zeta^2+r_s^2}}, \quad I_0^2 = \frac{\zeta}{\sqrt{\zeta^2+r_s^2}^3}, \quad I_0^3 = \frac{2\zeta^2-r_a^2}{\sqrt{\zeta^2+r_s^2}^5} \\ I_1^0 &= \frac{\sqrt{\zeta^2+r_s^2}-\zeta}{r_s}, \quad I_1^1 = \frac{1}{r} - \frac{\zeta}{r_s\sqrt{\zeta^2+r_s^2}}, \quad I_1^2 = \frac{r}{\sqrt{\zeta^2+r_s^2}^3}, \quad I_1^3 = \frac{3\zeta r}{\sqrt{\zeta^2+r_s^2}^5}. \end{aligned}\right\} \quad (A\,9)$$

Application of the steps outlined in this appendix to the inverse Fourier transform of (A 2) directly leads to (2.25) and (2.26).

The integration over the azimuthal angle γ in (3.5) lead to integrals of the type (Gradshteyn & Ryshik 1981, § 3.681)

$$\int_0^{\pi/2}\mathrm{d}\beta\frac{\sin^{2n}\beta\cos^{2m}\beta}{(1-k^2\sin^2\beta)^{(l+1/2)}} = \frac{1}{2}B(n+1/2, m+1/2)F(l+1/2, n+1/2, n+m+1, k^2). \quad (A\,10)$$

Using the three relations (Abramowitz & Stegun 1984, §§ 15.2.3 and 15.2.6)

$$\left(\frac{\mathrm{d}}{\mathrm{d}z}\right)^n z^{a+n-1}F(a,b,c;z) = \frac{\Gamma(a+n)}{\Gamma(a)}z^{a-1}F(a+n,b,c;z), \quad (A\,11a)$$

$$\left(\frac{\mathrm{d}}{\mathrm{d}z}\right)^n z^{b+n-1}F(a,b,c;z) = \frac{\Gamma(b+n)}{\Gamma(b)}z^{b-1}F(a,b+n,c;z), \quad (A\,11b)$$

$$\left(\frac{\mathrm{d}}{\mathrm{d}z}\right)^n (1-z)^{a+b-c}F(a,b,c;z) = \frac{\Gamma(c-a+n)\Gamma(c-b+n)\Gamma(c)}{\Gamma(c-a)\Gamma(c-b)\Gamma(c+n)} \times(1-z)^{a+b-c-n}F(a,b,c+n;z), \quad (A\,11c)$$

the hypergeometric function can be written as a derivative of the complete elliptic integral of the first kind:

$$K(k) = \int_0^{\pi/2}\frac{\mathrm{d}\beta}{\sqrt{1-k^2\sin^2\beta}} = \frac{\pi}{2}F(1/2, 1/2, 1, k^2). \quad (A\,12)$$

Derivatives for complete elliptic functions are given in Gradshteyn & Ryshik (1981, § 8.123). The integral for o_{s02}^M and $\bar{o}_{s20}^M$ also involves the complete elliptic integral of the third kind. We find

$$\bar{o}_{00}^M = \frac{6}{d_{pm}}K'\left(\frac{d_{mm}}{d_{pm}}\right) - \frac{2(z-h)^2}{d_{pm}d_{mm}^2}E'\left(\frac{d_{mm}}{d_{pm}}\right) + \left(-\frac{6}{d_{pp}} + \frac{4zh(z+h)^2}{d_{pp}^3 d_{mp}^2}\right)K'\left(\frac{d_{mp}}{d_{pp}}\right) + \left(\frac{2z^2+2h^2+8zh}{d_{pp}d_{mp}^2} - \frac{8zh(z+h)^2}{d_{pp}^3 d_{mp}^2} - \frac{8zh(z+h)^2}{d_{pp}d_{mp}^4}\right)E'\left(\frac{d_{mp}}{d_{pp}}\right), \quad (A\,13)$$

$$\bar{o}^M_{s00} = \boldsymbol{T}_B \left\{ \frac{8}{d_{pp}} K' \left(\frac{d_{mp}}{d_{pp}} \right) \right\}, \tag{A 14}$$

$$\begin{aligned}\bar{o}^M_{01} = {} & \frac{2\sqrt{2}(z-h)(x_s - x'_s)}{d_{pm} d^2_{mm}} E' \left(\frac{d_{mm}}{d_{pm}} \right) - \frac{4\sqrt{2} x_s (z-h)}{d^3_{pm}} D' \left(\frac{d_{mm}}{d_{pm}} \right) \\ & + \left(\frac{-2\sqrt{2}(z-h)(x_s - x'_s)}{d_{pp} d^2_{mp}} - \frac{8\sqrt{2} z h (z+h)(x_s - x'_s)}{d_{pp} d^4_{mp}} + \frac{8\sqrt{2} z h (z+h) x'_s}{d^3_{pp} d^2_{mp}} \right) \\ & \times E' \left(\frac{d_{mp}}{d_{pp}} \right) + \left(\frac{4\sqrt{2} x (z-h)}{d^3_{pp}} + \frac{8\sqrt{2} z h x_s (z+h)}{d^5_{pp}} \right) D' \left(\frac{d_{mp}}{d_{pp}} \right) \\ & + \frac{4\sqrt{2} z h (z+h)(x_s - x'_s)}{d^3_{pp} d^2_{mp}} K' \left(\frac{d_{mp}}{d_{pp}} \right), \end{aligned} \tag{A 15}$$

$$\begin{aligned}\bar{o}^M_{02} = {} & \frac{2}{d_{pm}} K' \left(\frac{d_{mm}}{d_{pm}} \right) - \frac{16 x_s^2}{d^3_{pm}} \left(2C' \left(\frac{d_{mm}}{d_{pm}} \right) - D' \left(\frac{d_{mm}}{d_{pm}} \right) \right) - \frac{2(z-h)^2}{d_{pm} d^2_{mm}} E' \left(\frac{d_{mm}}{d_{pm}} \right) \\ & + \left[-\frac{2}{d_{pp}} + \frac{4 z h (z+h)^2}{d^2_{mp} d^3_{pp}} \right] K' \left(\frac{d_{mp}}{d_{pp}} \right) + \frac{16 x_s^2}{d^3_{pp}} \left(2C' \left(\frac{d_{mp}}{d_{pp}} \right) - D' \left(\frac{d_{mp}}{d_{pp}} \right) \right) \\ & + \frac{64 x_s^2 z h}{d^2_{mp} d^3_{pp}} \left[C' \left(\frac{d_{mp}}{d_{pp}} \right) - D' \left(\frac{d_{mp}}{d_{pp}} \right) \right] + \left(\frac{2(z^2 + h^2 + 8zh)}{d_{pp} d^2_{mp}} - \frac{8 z h (z+h)^2}{d^3_{pp} d^2_{mp}} \right. \\ & \left. - \frac{8 z h (z+h)^2}{d_{pp} d^4_{mp}} \right) E' \left(\frac{d_{mp}}{d_{pp}} \right), \end{aligned} \tag{A 16}$$

$$\begin{aligned}\bar{o}^M_{s02} = {} & \boldsymbol{T}_B \left\{ \left(-\frac{8 x_s^2}{d_{pp} x'^2_s} - \frac{8\left(x_s^2 - x'^2_s\right)(|z| + |h|)^2}{d_{pp} (x_s + x'_s)^2 x'^2_s} \right) K' \left(\frac{d_{mp}}{d_{pp}} \right) + 8 \frac{d_{pp}}{x'^2_s} E' \left(\frac{d_{mp}}{d_{pp}} \right) \right. \\ & - 4 \frac{\pi(|z| + |h|)}{x'^2_s} - 8 \frac{|z| + |h|}{x'^2_s} \operatorname{sign}\left(x_s^2 - x'^2_s\right) \left(F \left(\frac{|x_s - x'_s| d_{pp}}{(x_s + x'_s) d_{mp}}, \frac{d_{mp}}{d_{pp}} \right) \left[K' \left(\frac{d_{mp}}{d_{pp}} \right) \right. \right. \\ & \left. \left. - E' \left(\frac{d_{mp}}{d_{pp}} \right) \right] - E \left(\frac{|x_s - x'_s| d_{pp}}{(x_s + x'_s) d_{mp}}, \frac{d_{mp}}{d_{pp}} \right) K' \left(\frac{d_{mp}}{d_{pp}} \right) \right) \Bigg\}, \end{aligned} \tag{A 17}$$

$$\begin{aligned}\bar{o}^M_{11} = {} & \frac{8\left(x_s^2 + x'^2_s\right)}{d^3_{pm}} D' \left(\frac{d_{mm}}{d_{pm}} \right) + \left(-\frac{4}{d_{pm}} + \frac{4(z-h)^2}{d_{pm} d^2_{mm}} \right) E' \left(\frac{d_{mm}}{d_{pm}} \right) \\ & + \left(\frac{-8\left(x_s^2 + x'^2_s + 2zh\right)}{d^3_{pp}} + \frac{32 x_s x'_s z h (z+h)^2}{d^5_{pp} d^2_{mp}} + \frac{16 z h (z+h)^2}{d^5_{pp}} \right) D' \left(\frac{d_{mp}}{d_{pp}} \right) \\ & + \left(\frac{4}{d_{pp}} - \frac{4(z^2 + h^2)}{d_{pp} d^2_{mp}} + \frac{8 z h (z+h)^2}{d^3_{pp} d^2_{mp}} - \frac{16 z h (z+h)^2}{d_{pp} d^4_{mp}} \right) E' \left(\frac{d_{mp}}{d_{pp}} \right), \end{aligned} \tag{A 18}$$

$$\begin{aligned}\bar{o}^M_{12} = {} & \frac{-16\sqrt{2} x_s (z-h)\left(x'^2_s + 2x_s{}^2 + 2(z-h)^2\right)}{d^5_{pm}} C' \left(\frac{d_{mm}}{d_{pm}} \right) \\ & + \left(\frac{2\sqrt{2}(z-h)(x_s - x'_s)}{d^2_{mm} d_{pm}} + \frac{2\sqrt{2}(z-h)(4x_s + x'_s)}{d^3_{pm}} \right) E' \left(\frac{d_{mm}}{d_{pm}} \right) \end{aligned}$$

$$+\left(\frac{16\sqrt{2}x_s(z-h)\left(x_s'^2+2x_s^2+2(z+h)^2\right)}{d_{pp}^5}+\frac{64\sqrt{2}x_szh(z+h)}{d_{pp}^5}\right)C'\left(\frac{d_{mp}}{d_{pp}}\right)$$
$$+\left(-\frac{2\sqrt{2}(z-h)(x_s-x_s')}{d_{mp}^2d_{pp}}-\frac{2\sqrt{2}(z-h)(4x_s+x_s')}{d_{pp}^3}-\frac{24\sqrt{2}x_szh(z+h)}{d_{mp}^2d_{pp}^3}\right.$$
$$\left.+\frac{8\sqrt{2}zh(z+h)(x_s-x_s')}{d_{mp}^4d_{pp}}\right)E'\left(\frac{d_{mp}}{d_{pp}}\right)-\frac{4\sqrt{2}(x_s-x_s')zh(z+h)}{d_{mp}^2d_{pp}^3}K'\left(\frac{d_{mp}}{d_{pp}}\right)$$
$$+\frac{8\sqrt{2}zh(z+h)x_s'}{d_{pp}^5}D'\left(\frac{d_{mp}}{d_{pp}}\right), \tag{A 19}$$

$$\bar{o}_{22}^M=\frac{6}{d_{pm}}K'\left(\frac{d_{mm}}{d_{pm}}\right)+16\left(\frac{2}{d_{pm}}+\frac{(z-h)^2}{d_{pm}^3}\right)\left(C'\left(\frac{d_{mm}}{d_{pm}}\right)-D'\left(\frac{d_{mm}}{d_{pm}}\right)\right)$$
$$+\frac{16(z-h)^2}{d_{pm}^3}C'\left(\frac{d_{mm}}{d_{pm}}\right)-\frac{2(z-h)^2}{d_{pm}d_{mm}^2}E'\left(\frac{d_{mm}}{d_{pm}}\right)+\left(-\frac{6}{d_{pp}}+\frac{4zh(z+h)^2}{d_{pp}^3d_{mp}^2}\right)$$
$$\times K'\left(\frac{d_{mp}}{d_{pp}}\right)+\left(\frac{2z^2+2h^2+8zh}{d_{pp}d_{mp}^2}-\frac{8zh(z+h)^2}{d_{pp}^3d_{mp}^2}-\frac{8zh(z+h)^2}{d_{pp}d_{mp}^4}\right)E'\left(\frac{d_{mp}}{d_{pp}}\right)$$
$$-16\frac{z^2+4zh+h^2}{d_{pp}^3}C'\left(\frac{d_{mp}}{d_{pp}}\right)-16\left(\frac{2}{d_{pp}}+\frac{z^2+4zh+h^2}{d_{pp}^3}+\frac{4zh(z+h)^2}{d_{mp}^2d_{pp}^3}\right)$$
$$\times\left(C'\left(\frac{d_{mp}}{d_{pp}}\right)-D'\left(\frac{d_{mp}}{d_{pp}}\right)\right), \tag{A 20}$$

$$\bar{o}_{s22}^M=\boldsymbol{T}_B\left\{\frac{8}{d_{pp}}K'\left(\frac{d_{mp}}{d_{pp}}\right)+\frac{128}{3d_{pp}}\left(C'\left(\frac{d_{mp}}{d_{pp}}\right)-D'\left(\frac{d_{mp}}{d_{pp}}\right)\right)\right\}, \tag{A 21}$$

where

$$\left.\begin{aligned}&d_{pm}=\sqrt{(x_s+x_s')^2+(z-h)^2},\quad d_{mm}=\sqrt{(x_s-x_s')^2+(z-h)^2},\\&d_{mp}=\sqrt{(x_s-x_s')^2+(|z|+|h|)^2},\quad d_{pp}=\sqrt{(x_s+x_s')^2+(|z|+|h|)^2}.\end{aligned}\right\} \tag{A 22}$$

$E(x,k)$ and $F(x,k)$ are the incomplete elliptic integrals of the first and second kind, $E'(k)$ and $K'(k)$ the complementary complete elliptic integrals of the first and second kind; and $D'(k)=(K'(k)-E'(k))/(1-k^2)$, and $C'(k)=(D'(k)-E'(k)/2)/(1-k^2)$ are linear combinations of E' and K' that do not exhibit singularities near $k=1$. The remaining components of Oseen's tensor are found from the symmetry relation:

$$\bar{o}_{ij}^M(x_s,z\,|\,x_s',h)=\bar{o}_{ji}^M(x_s',h\,|\,x_s,z). \tag{A 23}$$

The expression for the surface Oseen tensor for $\mathscr{B}\to\infty$ is obtained by using the identity (A 5) for the operator $\boldsymbol{T}_B$:

$$\lim_{\mathscr{B}\to\infty}\bar{o}_{s00}^M=\lim_{\mathscr{B}\to\infty}\int_0^\infty \mathrm{d}t\,\mathrm{e}^{-t}\frac{8}{\sqrt{(x_s+x_s')^2+(|z|+|h|+\mathscr{B}at)^2}}K'(1)$$
$$=\lim_{\mathscr{B}\to\infty}\frac{4\pi}{\mathscr{B}a}\mathrm{e}^{\frac{|z|+|h|}{\mathscr{B}a}}\int_{\frac{|z|+|h|}{\mathscr{B}a}}^\infty \mathrm{d}t\,\mathrm{e}^{-t}\frac{8}{\sqrt{\dfrac{(x_s+x_s')^2}{(\mathscr{B}a)^2}+t^2}}$$

$$= \lim_{\mathscr{B}\to\infty} \frac{4\pi}{\mathscr{B}a}\left[\pi/2\left(\boldsymbol{H}_0\left(\frac{x_s+x_s'}{\mathscr{B}a}\right)-N_0\left(\frac{x_s+x_s'}{\mathscr{B}a}\right)\right)-\int_0^{\frac{|z|+|h|}{\mathscr{B}a}} \mathrm{d}t\,\frac{\mathrm{e}^{-t}}{\sqrt{\frac{(x_s+x_s')^2}{(\mathscr{B}a)^2}+t^2}}\right]$$

$$= \lim_{\mathscr{B}\to\infty} \frac{4\pi}{\mathscr{B}a}\left[-\ln\left(\frac{x_s+x_s'}{2\mathscr{B}a}\right)-\gamma-\int_0^{\frac{|z|+|h|}{\mathscr{B}a}} \mathrm{d}t\,\frac{1}{\sqrt{\frac{(x_s+x_s')^2}{(\mathscr{B}a)^2}+t^2}}\right]$$

$$= \frac{4\pi}{\mathscr{B}a}\left[\ln\left(\frac{2\mathscr{B}a}{x_s+x_s'}\right)-\gamma-\operatorname{arsinh}\left(\frac{|z|+|h|}{x_s+x_s'}\right)\right]$$

$$= \frac{4\pi}{\mathscr{B}a}\left[\ln\frac{2\mathscr{B}a}{|z|+|h|+\sqrt{(x_s+x_s')^2+(|z|+|h|)^2}}-\gamma\right] \tag{A 24}$$

which is identical to the first line of (4.1). The second line of (4.1) is obtained along analogues steps. Setting $x_s + x_s' = 0$ in the second line in (A 24) leads to the result (4.4) given for $\lim_{a\to 0} \bar{o}_{s00}^{M}$ when $z + h > a$.

Appendix B. Numerics

The axial Oseen tensor $\bar{\boldsymbol{O}}^{M}(x_s, z|x_s', h)$ has logarithmic singularities for $x_s = x_s'$ $z = h$, which disappear after integration over the force profile. When discretizing the problem, that is, setting

$$\boldsymbol{f}(h) = \boldsymbol{f}_s \quad \text{for} \quad h_s - \zeta/2 < h < h_s + \zeta/2 \tag{B 1}$$

a simple way of tackling these singularities is to replace the d_{mm} (equation (A 22)) in equations (15)–(A 20) by

$$d_{mm}^{\zeta} = \sqrt{(x_s - x_s')^2 + (z-h)^2 + \frac{\zeta^2(1+(\mathrm{d}\rho/\mathrm{d}z)^2)}{\mathrm{e}^3}}. \tag{B 2}$$

This removes the singularities and we can approximate the integral (3.7) by

$$\rho_r \zeta u_{i,r} = A_{ij,rs} f_{j,s}, \tag{B 3}$$

where $A_{ij,rs}$ is a matrix given by

$$\begin{aligned} A_{ij,rs} &= \int_{z_r-\zeta/2}^{z_r+\zeta/2}\int_{h_s-\zeta/2}^{h_s+\zeta/2} \rho(z)\bar{\boldsymbol{O}}_{ij}(\rho(z), z|\rho(h), h)\rho(h)\,\mathrm{d}z\,\mathrm{d}h \\ &\approx \zeta^2\rho_r\rho_s\bar{\boldsymbol{O}}_{ij}^{\zeta}(\rho(z_r), z_r\big|\rho(h_s), h_s) \end{aligned} \tag{B 4}$$

and $\bar{\boldsymbol{O}}_{ij}^{\zeta}$ is the Oseen tensor with argument d_{mm}^{ζ} instead of d_{mm}. The matrix $\boldsymbol{A}$ is symmetric and numerical inversion then yields the force profile:

$$f_{j,s} = (\boldsymbol{A}^{-1})_{ji,sr}\rho_r\zeta u_{i,r}. \tag{B 5}$$

The derivatives of the surface Oseen tensor components (A 14), (A 17) and (A 21) with respect to $|z|$ occurring in the Taylor expansion are performed numerically. The inversion of equation (4.12*b*) is then analogous to that of (4.12*a*).

REFERENCES

Abramowitz, M. & Stegun, I. A. 1984 *Pocketbook of Mathematical Functions*. Verlag Harri Deutsch, Frankfurt/Main, Germany.

Danov, K., Aust, R., Durst, F. & Lange, U. 1995 Influence of the Surface shear viscosity on the hydrodynamic resistance and surface diffusivity of a large Brownian particle. *J. Colloid Interface Sci.* **175**, 36–45.

Danov, K., Dimova, R. & Pouligny, B. 2000 Viscous drag of a solid sphere straddling a spherical or flat surface. *Phys. Fluids* **12**, 2711–2722.

Danov, K. D., Kralchevsky, P. A. & Boneva, M. P. 2004 Electrodipping force acting on solid particles at a fluid interface. *Langmuir* **20**, 6139–6151.

Dimova, R., Dietrich, C., Hadjiisky, A., Danov, K. & Pouligny, B. 1999*a* Falling ball viscosimetry of giant vesicle membranes: finite-size effects. *Eur. Phys. J.* B **12**, 589–598.

Dimova, R., Dietrich, C. & Pouligny, B. 1999*b* Motion of particles attached to giant vesicles: falling ball viscosimetry and elasticity measurements on lipid membranes. In *Giant Vesicles* (ed. P. Walde & P. Luisi), Chap. 15, p. 221. John Wiley & Sons.

Dimova, R., Danov, K., Pouligny, B. & Ivanov, I. B. 2000 Drag of a solid particle trapped in a thin film or at an interface, influence of the surface viscosity and elasticity. *J. Colloid Interface Sci.* **226**, 35–43.

Dussan, V., E. B. & Davis, S. H. 1974 Motion of a fluid-fluid interface along a solid-surface. *J. Fluid Mech.* **65**, 71–95.

Faxen, H. 1923 Die Bewegung einer starren Kugel längs der Achse eines mit zäher Flüssigkeit gefüllten Rohres. *Arkiv. Mat. Astron. Fys.* **17**, No. 27.

Fischer, Th. M. 2003 The drag on needles moving in a Langmuir monolayer. *J. Fluid Mech.* **498**, 123–137.

Fischer, Th. M. 2004 Comment on: "Shear viscosity of Langmuir monolayers in the low-density limit". *Phys. Rev. Lett.* **92**, 139603.

Forstner, M. B., Käs, J. A. & Martin, D. S. 2001 Single lipid diffusion in Langmuir monolayers. *Langmuir* **17**, 567–570.

Forstner, M. B., Martin, D. S., Navar, A. M. & Käs, J. A. 2003 Simultaneous single-particle tracking and visualization of domain structure on lipid monolayers. *Langmuir* **19**, 4876–4879.

Gradshteyn, I. S. & Ryshik, I. M. 1981 *Tables of Series, Products, and Integrals*. Harri Deutsch, Thun, Frankfurt/Main, Germany.

Happel, J. & Brenner, H. 1983 *Low Reynolds Number Hydrodynamics*. Martinus Nijhoff, The Hague.

Hughes, B. D., Pailthorpe, B. A. & White, L. R. 1981 The translational and rotational drag on a cylinder moving in a membrane. *J. Fluid Mech.* **110**, 349–372.

Huh, C. & Scriven, L. I. 1971 Hydrodynamic model of steady movement of a solid/liquid/fluid contact line. *J. Colloid Interface Sci.* **35**, 85–101.

Klingler, J. F. & McConnell, H. 1993 Brownian-motion and fluid-mechanics of lipid monolayer domains. *J. Phys. Chem.* **97**, 6096–6100.

Levine, A. J. & MacKintosh, F. C. 2002 Dynamics of viscoelastic membranes. *Phys. Rev.* E **66**, 061606.

Manneville, J.-B., Etienne-Manneville, S., Skehel, P., Carter, T., Ogden, D. & Ferenczi, M. 2003 Interaction of the actin cytoskeleton with microtubules regulates the secretory organelle movement near the plasma membrane in human endothelial cells. *J. Cell. Sci.* **116**, 3927–3938.

Mercier, F., Reggio, R., Devilliers, G., Bataille, D. & Mangeat, P. 1989 Membrane-cytoskeleton dynamics in rat parietal cells: mobilization of actin and spectrin upon stimulation of gastric acid secretion. *J. Cell Biol.* **108**, 441–453.

O'Neill, M. E., Ranger, K. B. & Brenner, H. 1986 Slip at the surface of a translating-rotating sphere bisected by a free surface bounding a semi-infinite viscous fluid: Removal of the contact-line singularity. *Phys. Fluids* **29**, 913–924.

Nikolaides, M. G., Bausch, A. R., Hsu, M. F., Dinsmore, A. D., Brenner, M. P. & Weitz, D. A. 2002 Electric-field-induced capillary attraction between like-charged particles at liquid interfaces. *Nature* **420**, 299–301.

Oh, S. G. & Slattery, J. C. 1978 Disk and binocal interfacial viscosimeters. *J. Colloid Interface Sci.* **67**, 516–525.

Peters, R. & Cherry, R. J. 1982 Lateral and rotational diffusion of bacteriorhodopsin in lipid bilayers: Experimental test of Saffman-Delbrück equations. *Proc. Natl Acad. Sci. USA* **79**, 4317–4321.

Petkov, J. T., Denkov, N. D., Danov, K., Velev, O. D., Aust, R. & Durst, F. 1995 Measurement of the drag coefficient of spherical particles attached to fluid interfaces. *J. Colloid Interface Sci.* **172**, 147–154.

Pralle, A., Keller, P., Florin, E. L., Simons, K. & Horber, J. K. H. 2000 Sphingolipid-cholesterol rafts diffuse as small entities in the plasma membrane of mammalian cells. *J. Cell. Biol.* **148** 997–1007.

Russel, W. B., Saville, D. A. & Schowalter, W. R. 1989 *Colloidal Dispersions*, pp. 31–35. Cambridge University Press.

Saffman, P. G. & Delbrück, M. 1975 Brownian-motion in biological-membranes. *Proc. Natl Acad. Sci. USA* **72,** 3111–3113.

Schwartz, D., Knobler, C. M. & Bruinsma, R. 1994 Direct observation of Langmuir monolayer flow-through a channel. *Phys. Rev. Lett.* **73**, 2841–2844.

Sickert, M. & Rondelez, F. 2003 Shear viscosity of Langmuir monolayers in the low-density limit. *Phys. Rev. Lett.* **90**, 126104.

Sickert, M. & Rondelez, F. 2004 Comment on "Shear viscosity of Langmuir monolayers in the low-density limit" – reply. *Phys. Rev. Lett.* **92**, 139604.

Steffen, P., Heinig, P., Wurlitzer, S., Khattari, Z. & Fischer, Th. M. 2001 The translational and rotational drag on Langmuir monolayer domains. *J. Chem. Phys.* **115**, 994–997.

Stone, H. A. & Ajdari, A. 1998 Hydrodynamics of particles embedded in a flat surfactant layer overlying a subphase of finite depth. *J. Fluid Mech.* **369**, 151–173.

Wurlitzer, S., Schmiedel, H. & Fischer, Th. M. 2002 Electrophoretic relaxation dynamics of domains in Langmuir monolayers. *Langmuir* **18**, 4393–4400.